

Article

High-Temperature Behavior of CaO-FeO_x-Al₂O₃-SiO₂-Rich Alkali Activated Materials

Guilherme Ascensão^{1,2,3,4,*} , Flora Faleschini² , Maurizio Marchi³, Monica Segata³, Jorn Van De Sande^{4,5}, Hubert Rahier⁵ , Enrico Bernardo⁶  and Yiannis Pontikes⁴

- ¹ RISCO, Department of Civil Engineering, University of Aveiro, 3810-193 Aveiro, Portugal
² Department of Civil, Environmental and Architectural Engineering, University of Padova, Via Marzolo, 9, 35131 Padova, Italy; flora.faleschini@dicea.unipd.it
³ HeidelbergCement Group, Italcementi S.p.A, Via Stezzano, 87, 24126 Bergamo, Italy; m.marchi@italcementi.it (M.M.); m.segata@italcementi.it (M.S.)
⁴ Department of Materials Engineering, KU Leuven, Kasteelpark Arenberg, 44, 3001 Leuven, Belgium; jorn.van.de.sande@vub.be (J.V.D.S.); yiannis.pontikes@kuleuven.be (Y.P.)
⁵ Department of Physical Chemistry and Polymer Science, Vrije Universiteit Brussel, Pleinlaan 2, 1050 Brussels, Belgium; hubert.rahier@vub.be
⁶ Department of Industrial Engineering, University of Padova, 35131 Padova, Italy; enrico.bernardo@unipd.it
* Correspondence: guilhermeascensao@ua.pt; Tel.: +35-19-6694-4248

Abstract: Alkali-activated materials (AAMs) provide an opportunity to up-cycle several residues into added-value materials. Although generally praised for their performance under thermal loads, the thermal behavior of AAMs is dictated by a multitude of factors and the performance of CaO-FeO_x-rich systems may differ from geopolymers. Therefore, this work ascertains the high-temperature resistance of CaO-FeO_x-Al₂O₃-SiO₂-rich AAMs. Mortars were exposed to different heating rates (≤ 10 °C/min) and temperatures (≤ 1100 °C), and volume and mass loss, apparent density, compressive strength (CS), mineralogical composition, and morphology were evaluated. At low heating rates, the main effects noted were densification and a gradual lightening of color as the temperature rose. CS underwent an abrupt decline at 750 °C and recovered at higher temperatures, reaching a maximum value of 184 ± 13 MPa at 1100 °C. With an increased heating rate to 10 °C/min, the strength loss at 750 °C persisted, but maximum CS was halved when firing at 900 °C. At 1100 °C, a significant reduction of CS was observed, but all samples maintained their integrity. Except for 1100 °C at 10 °C/min, all sintered-AAMs presented residual CS above 40 MPa. These results demonstrate that CaO-FeO_x-Al₂O₃-SiO₂-rich AAMs present interesting thermal behavior and can be potentially used to produce glass-ceramics or refractory materials from secondary resources.



Citation: Ascensão, G.; Faleschini, F.; Marchi, M.; Segata, M.; Van De Sande, J.; Rahier, H.; Bernardo, E.; Pontikes, Y. High-Temperature Behavior of CaO-FeO_x-Al₂O₃-SiO₂-Rich Alkali Activated Materials. *Appl. Sci.* **2022**, *12*, 2572. <https://doi.org/10.3390/app12052572>

Academic Editor: Doo-Yeol Yoo

Received: 7 January 2022

Accepted: 25 February 2022

Published: 1 March 2022

Publisher's Note: MDPI stays neutral with regard to jurisdictional claims in published maps and institutional affiliations.



Copyright: © 2022 by the authors. Licensee MDPI, Basel, Switzerland. This article is an open access article distributed under the terms and conditions of the Creative Commons Attribution (CC BY) license (<https://creativecommons.org/licenses/by/4.0/>).

Keywords: alkali activated materials; high-temperature behavior; secondary resources

1. Introduction

Increasing the use of alternative feedstock materials is crucial to reduce the current pressure on natural resources and to diminish the environmental impact of our industrial sectors. Moreover, using low-grade materials and residues as raw materials also represents an important and long identified economic opportunity for manufacturers. In the field of secondary resources, thermochemical conversion processes belong to a group of emerging technologies that aim to reclaim large volumes of low-value materials—such as industrial, municipal, and even mined solid wastes from historical landfills—and reintroduce them into materials' cycles in the form of added-value materials. The primary outputs of these processes are valuable energy carriers and metals, but an inorganic solid material is also generated. This inorganic fraction is molten and often vitrified by water quenching, afterwards being either disposed of or used in low-value applications (e.g., road paving). As thermochemical conversion processes continue to thrive, and their worldwide

implementation grows, the volumes of these vitrified residues are expected to increase. The development of added-value products using such secondary outputs can have a remarkably positive effect on the sustainability of thermochemical technologies themselves, either directly, by providing a supplementary value stream, or indirectly, by abolishing associated environmental impacts and costs related to landfill. The use of such residues as precursors in the production of alkali-activated materials (AAMs) has been identified as a promising valorization route and suggested applications include, among others, pavers [1], mortars [2], and insulating building materials [3]. Another attractive property of AAMs is their performance at high temperatures. Unlike concrete, which suffers considerable degradation and spalling even below 400 °C [4,5], the physico-chemical characteristics of AAMs allow them to act as fire spreading and thermal energy barriers that prevent failure of construction elements. Yet, the thermal behavior of AAMs depend on several synthesis conditions, such as the chemical composition of the parent precursors, the type (silicate or hydroxide solutions), concentration, and charge balancing cation (Na^+ or K^+) in the activating solution, and Si/Al molar ratio [6,7]. The synthesis conditions dictate the pore structure and liquidus temperature of AAMs, as well as the amount and type of crystalline phases formed. Depending on their characteristics, the use of additives can also have a significant thermodynamic impact when firing alkali-activated materials.

The typical chemical composition of the slag produced during the thermochemical conversion of municipal and mined wastes can be described as a $\text{CaO-FeO}_x\text{-Al}_2\text{O}_3\text{-SiO}_2$ quaternary system, which sometimes also contains a significant MgO content [8]. This chemical composition could be adjusted to promote the formation of more refractory phases upon thermal exposure, i.e., by adding alumina-rich materials [7,9,10], but changing the composition of such low-value raw material may entail undesirable environmental and economic costs. Considering the above, the present work did not aim to enhance the thermal properties of $\text{CaO-FeO}_x\text{-Al}_2\text{O}_3\text{-SiO}_2$ -rich AAMs by altering their chemical composition with beneficial admixtures but rather to characterize the thermal performance of potassium-based AAMs previously optimized for general construction purposes. Thus, the thermal performance of conventional construction materials such as OPC-concrete, and not fire-resistant or refractory ones, should be used as a benchmark throughout this work.

Pure $(\text{Na}_2\text{O}/\text{K}_2\text{O})\text{-Al}_2\text{O}_3\text{-SiO}_2$ ternary systems are known to present excellent thermal resistance due to the crystallization of feldspar and feldspathoid phases, i.e., framework aluminosilicates, featuring various proportions of both SiO_4 and AlO_4 units, the latter being stabilized by alkali ions. These phases comprise albite (Na feldspar, $\text{NaAlSi}_3\text{O}_8$ or $\text{Na}_2\text{O}\cdot\text{Al}_2\text{O}_3\cdot 6\text{SiO}_2$, having a liquidus temperature, 1118 °C), nepheline (Na-K feldspathoid, $\text{Na}_3\text{KAl}_4\text{Si}_4\text{O}_{16}$, stable up to 1256 °C), and carnegieite (Na feldspathoid, NaAlSiO_4 or $\text{Na}_2\text{O}\cdot\text{Al}_2\text{O}_3\cdot 2\text{SiO}_2$, having a liquidus temperature, 1526 °C) in the case of sodium-based activators. In the case of potassium-based activators, the developed aluminosilicate compounds exhibit even higher melting points, as in the case of orthoclase (K feldspar, KAlSi_3O_8 or $\text{K}_2\text{O}\cdot\text{Al}_2\text{O}_3\cdot 6\text{SiO}_2$, having a liquidus temperature of 1250 °C), leucite (K feldspathoid, KAlSi_2O_6 or $\text{Na}_2\text{O}\cdot\text{Al}_2\text{O}_3\cdot 4\text{SiO}_2$, with a congruent melting point of 1693 °C), and kalsilite (K feldspathoid, KAlSiO_4 or $\text{K}_2\text{O}\cdot\text{Al}_2\text{O}_3\cdot 2\text{SiO}_2$, having a liquidus temperature, 1750 °C) [10].

The refractory performance of potassium-based ternary systems further benefits from the higher viscosity of potassium melts. This reduces deformation due to flow and reinforces the advantageous character of potassium-based AAMs for high-temperature applications. Nevertheless, it should be mentioned that $\text{Na}_2\text{O-SiO}_2\text{-Al}_2\text{O}_3$ systems can also present excellent resistance to high temperature if a specific set of synthesis conditions that promote carnegieite formation (melting point, 1526 °C) are provided. On the other hand, $\text{K}_2\text{O-SiO}_2\text{-Al}_2\text{O}_3$ systems present a broader set of synthesis conditions where refractory phases are formed upon sintering [10], and this is particularly relevant in industrial contexts where versatile and resilient mixture designs are of utmost importance. From this point of view, the use of a potassium-based activating solution is advantageous both in terms of thermal performance and industrial processing.

The chemical composition of the slag produced in thermochemical conversion processes is characterized by the presence of significant calcium and iron content, which, however, have a direct influence on the phase composition and morphology of the material after heating. Low calcium systems (i.e., geopolymers) are generally preferable for producing high-temperature resistance AAMs as calcium reduces the liquidus temperature of $K_2O-SiO_2-Al_2O_3$ systems. Furthermore, the near absence of hydrated and chemically bonded water in those low-calcium structures [11,12] reduces the deleterious microstructural effects of dehydration, which results in more thermally stable AAMs. The presence of iron can, however, be deleterious to $K_2O-Al_2O_3-SiO_2$ systems, depending on the amount of alumina present in the systems [10]. If insufficient alumina is available, the iron compounds formed are characterized by much lower melting temperatures relative to their iron-free analogs. Hence, the thermal performance of AAMs made from $FeO_x-Al_2O_3-SiO_2$ precursors with low-aluminum content is expected to be significantly impaired relative to their iron-free equivalents. On the other hand, in alumina-rich $K_2O-Al_2O_3-SiO_2$ systems, the introduction of iron is not expected to preclude the crystallization of highly stable and refractory phases such as mullite, leucite, and kalsilite, and can even promote the crystallization of refractory hercynite [10]. The presence of these phases enhances the thermal resistance of AAMs made from alumina-rich $FeO_x-Al_2O_3-SiO_2$ precursors and are expected to deliver excellent fire-resistant properties [9,13].

Several authors have investigated the phase transitions and thermal characteristics of AAMs produced from precursors such as metakaolin and fly-ash, which can be mainly described as $Al_2O_3-SiO_2$ binary systems [14,15], and calcium or iron-rich ones, such as ground granulated blast furnace slag [15], ferronickel slag [9], and copper slags [7,16]. The thermal characteristics of more complex $CaO-FeO_x-Al_2O_3-SiO_2$ quaternary systems have not yet been thoroughly investigated. As discussed, calcium- and iron-containing phases will play vital roles in determining the thermal performance of those AAMs. Thus, examining the properties of $CaO-FeO_x-Al_2O_3-SiO_2$ -rich AAMs after thermal exposure (the sintered counterparts) is crucial to establish these AAMs as reliable temperature resistant materials, with a place in the market, and deliver a long-term, large-scale, up-cycling solution for $CaO-FeO_x-Al_2O_3-SiO_2$ -rich residues generated during thermochemical conversion processes.

2. Materials and Methods

2.1. Raw Material Characterization and Mortar Preparation

A synthetic granular slag was produced with a chemical composition that mimics the expected inert vitrified material produced during the thermochemical conversion of combustible components of municipal and mined solid wastes. The detailed description of its production process is provided by Machiels et al. [1,2]. X-ray fluorescence (Bruker AXS S8 Tiger spectrometer, Billerica, MA, USA) was used to determine the bulk chemical composition of the slag, which can be generally described as a $CaO-FeO_x-Al_2O_3-SiO_2$ quaternary system. The complete chemical composition of the slag is given in Table 1. The Fe oxidation state was quantified as described by Close et al. [17] and the iron phases were found to be predominantly in the bivalent oxidation state (92%).

Table 1. Chemical composition of the synthetic slag used as main raw material (% by mass).

	LOI	SiO ₂	CaO	FeO _x	Al ₂ O ₃	MgO	TiO ₂	K ₂ O	Na ₂ O	MnO	Fe ³⁺ /Fe _{total}
Synthetic slag	1.9	34.9	23.1	22.8	16.2	1.3	0.6	0.5	0.3	0.1	0.08

Aiming to deliver sustainable materials, the use of ordinary Portland cement and natural aggregates was completely avoided in the mortars' mix design; the vitreous slag was used both as the main precursor and aggregate. For this purpose, the granular slag was subjected to distinct pre-processing procedures to achieve different particle size distributions

according to the envisioned usage (Figure 1). Particle size distribution was determined using a laser particle analyzer (Malvern Mastersizer 3000, Malvern Panalytical, Malvern, UK). Finely powdered slag with a specific surface area of $1120 \text{ m}^2/\text{kg}$ (determined by the Brunauer–Emmett–Teller method, BET) and density of $2.97 \text{ g}/\text{cm}^3$ was used as the binders' main precursor (94.5 wt.% of binders' solid load). Silica fume (SF, Elkem, >95% SiO_2) with a BET specific surface area of approximately $22,200 \text{ m}^2/\text{kg}$ was used as an admixture to increase the availability of Si species and support strength development. Increasing the Si/Al ratio was also expected to promote the formation of highly thermally stable phases [14] and produce compact microstructures with low porosity levels after thermal exposure [18], thus improving the high-temperature resistance and residual strength of the produced materials. A potassium-based activating solution was used following a mix design previously optimized. Theoretical predictions [10] and empirical experimentations [6] in the available literature confirm the superior thermal performance of potassium-based AAMs relative to their sodium-based counterparts. Potassium hydroxide (14 M) and potassium silicate solutions (23.8 wt.% SiO_2 , 9.5 wt.% K_2O , and 66.7 wt.% H_2O) were prepared by dissolving potassium hydroxide beads and anhydrous potassium silicate in demineralized water. The water content in the activating solution was adjusted (0.68 $\text{SiO}_2/\text{K}_2\text{O}$ molar ratio and 83.4 wt.% H_2O) to achieve the pre-defined solid over liquid ratio (S/L) of 2.85 and molar ratios in the binder composition.

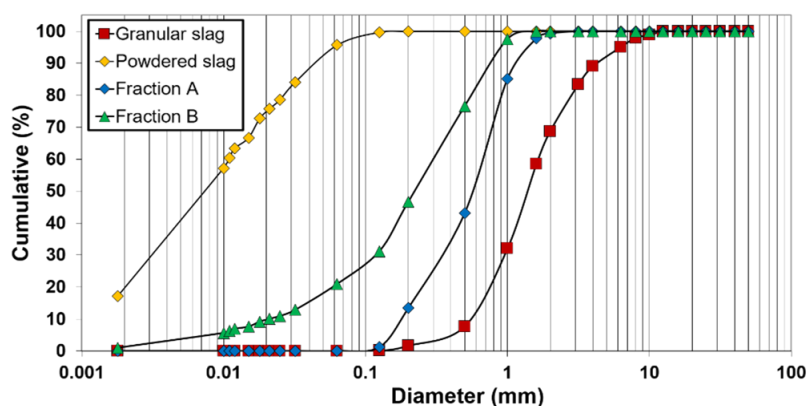


Figure 1. Particle size distribution of as-produced granular slag and after different pre-processing procedures. Powdered slag refers to finely milled slag used as binders' main precursor while fraction A and B designate roughly milled slags used as small size aggregates.

Based on our previous laboratory experimentation, the mortar mixture was designed for a binder-to-aggregate mass ratio of 0.88. Fuller distribution was applied to optimize aggregate particle size distribution (PSD). The PSD of the two fractions of the slag used as aggregates is shown in Figure 1. The density of the aggregate fractions was determined to be approximately $3.0 \pm 0.03 \text{ g}/\text{cm}^3$, and their mass ratio in the mortars' design was set to be 1.4:1. The characteristics of the reference mortar mix design are provided in Table 2.

Table 2. Reference mortar composition (wt.%).

Powdered Slag (PS)	Silica Fume (SF)	Solution	Aggregates	
			Fraction A	Fraction B
32.7	1.9	12.2	31.2	22.0

The mortars were produced following the procedure described by Ascensão et al. [19]. In short, it involved: (a) manually mixing the powdered slag and silica fume in a plastic container; (b) mixing the binders' solid components (PS+SF) and the alkaline solution at 140 rpm for 600 s in a mortar mixer (Testing Bluhm & Beuerherdt GmbH, Berlin, Germany);

and (c) mixing the pre-mixed aggregate fractions with the binder for 120 s at the same speed. The mortars were cast into $5 \times 5 \times 5 \text{ cm}^3$ metallic molds and cured for 24 h in controlled conditions ($20 \pm 0.5 \text{ }^\circ\text{C}$ and $95 \pm 1.0\%$ relative humidity). After demolding, the mortar specimens were individually sealed with a plastic film and thermally treated for 72 h at $50 \text{ }^\circ\text{C}$ and then kept at room conditions ($20 \pm 1.0 \text{ }^\circ\text{C}$ and $65 \pm 5.0\%$ relative humidity) until testing.

2.2. Methods

2.2.1. High-Temperature Processing

After 28 d of curing, mortar specimens were heated from room temperature up to $1100 \text{ }^\circ\text{C}$ in a chamber furnace (Carbolite RHF). Five different target temperatures were defined: 105, 600, 750, 900, and $1100 \text{ }^\circ\text{C}$. These target temperatures were chosen on the grounds of previous studies [5,7] that demonstrated the existence of relevant chemical transformations occurring in these temperature ranges. For each target temperature, a thermal profile with a heating rate of $1 \text{ }^\circ\text{C}/\text{min}$ [5,20,21] and an isothermal step of 1 h at the maximum temperature was followed. The heated specimens were left to cool down naturally inside the closed furnace. This procedure was replicated with a heating rate of $10 \text{ }^\circ\text{C}/\text{min}$ to assess the impact of heating rate on AAMs mineralogy, morphology, and post-heating properties. A minimum of two specimens per heating rate and maximum temperature were tested.

2.2.2. Physical-Mechanical Characterization

The weight (0.1-g accuracy) and dimensions (0.01-mm accuracy) of each specimen were measured before and after thermal exposure to evaluate the mass loss and the volumetric changes that occurred during thermal treatment (and eventual anisotropic features), respectively. The apparent density of the mortars was determined by the relation between the weight and volume of each sample. Compressive strength was determined using a Universal Testing Machine (Controls) according to EN196-1:2016 [22].

2.2.3. Crystallinity and Morphological Characterization

The crystallinity of the starting slag, silica fume, and mortars produced was assessed by X-ray diffraction (XRD), carried out on a conventional Bragg-Brentano Bruker D8 Advance diffractometer equipped with Lynxeye detector (Cu $K\alpha$ radiation $\lambda = 1.54059 \text{ \AA}$, divergence slit 0.5° , Soller slit set $2.5^\circ + 2.5^\circ$, $5\text{--}70^\circ$ 2θ , step/size 0.02° , and t/step 0.04 s) and phase identification by EVA software (database ICDD-PDF-2). Samples from green and thermally treated mortars were collected from mechanical tests, then ground, sieved ($\leq 45 \mu\text{m}$), and kept sealed prior to testing. Scanning electron microscopy (SEM—EVO[®] MA 15) equipped with energy dispersive X-ray spectrometry (EDS, AZtecEnergy, Karnataka, India) was used to further evaluate the differences in each sample's morphology before and after thermal exposure. All backscattered electron images (BSE) were acquired using a 20-kV acceleration voltage and a working distance of 10.0 mm.

3. Results and Discussion

3.1. Physical-Mechanical Characterization

The AAMs' residual properties were characterized as a function of temperature (up to $1100 \text{ }^\circ\text{C}$) and heating rate (1 and $10 \text{ }^\circ\text{C}/\text{min}$). Figure 2 illustrates the color change, cracking, and deformation of the mortars after high-temperature exposure. Below $750 \text{ }^\circ\text{C}$, there were no visible effects on the surface of the specimens independent of the heating rate used. Similar observations have been made by Khan et al. [23] in fly ash/GGBFS mortars. Only a slight lightening of the color could be observed from $20 \text{ }^\circ\text{C}$ (Figure 2a) to $600 \text{ }^\circ\text{C}$ (Figure 2b), which can be attributed to gradual dehydration and some Fe oxidation as shown by Rickard et al. [24]. In fact, Figure 3 shows that mass loss mainly occurred in this temperature range. The mass loss at $105 \text{ }^\circ\text{C}$ can be attributed to the evaporation of free water located in existing pores. Previous works [7] have reported a higher mass loss

in this temperature range, which can be explained—along with the differences in binder chemistry—by the curing conditions (50 °C for 3 d) and curing duration (28 d) prior to thermal testing employed in this work. Thus, part of the water has already evaporated before the experiment when following this procedure. The further mass loss observed at temperatures up to 600 °C can be attributed to the egress of water present in smaller sized pores, interstitial water, and chemically bonded water in hydroxyl groups [11,14]. No anisotropic features were detected, and a uniform volumetric contraction that did not exceed 20 vol% was observed. Rickard et al. [24] reported significant lower shrinkage values in Fe-rich AAMS (3% at 900 °C) while He et al. [25] refer to shrinkage values of 5% in FA geopolymers fired at temperature of 800 °C. The influence of the heating rate started to become evident from 750 °C, as shown in Figure 2c–h. The specimens heated at lower rates (1 °C/min) changed color from a light grey to a gradually more brownish and yellow color (see Figure 2c,e,g). No cracks were visible on the surfaces of these samples, and the absence of color gradients indicates uniform mineralogical transformations [24]. The mineralogical transformations that occurred at these temperatures explain the changes in color and are discussed later in this work.

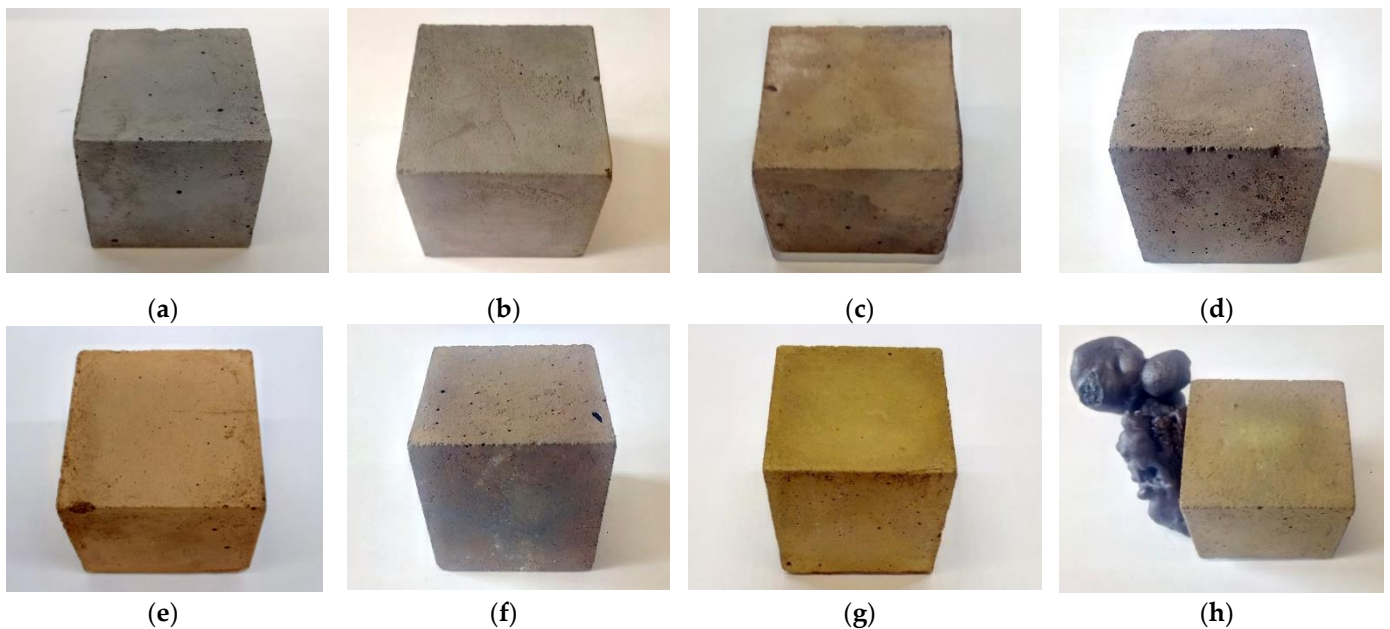


Figure 2. Alkali activated mortar specimens after 28 d of curing and thermal exposure to: (a) 20 °C; (b) 600 °C; (c,d) 750 °C with heating rates of 1 and 10 °C/min, respectively; (e,f) 900 °C with heating rates of 1 and 10 °C/min, respectively; (g,h) 1100 °C with heating rates of 1 and 10 °C/min, respectively. Mortars exposed to 105 °C are not shown here, but no significant modifications of specimens' appearance could be seen relative to the ones kept at 20 and 600 °C (a). At 600 °C there were no visible differences between specimens heated with distinct heating rates, with (b) being a representative example of both. Molten material at the surface of mortars heated up to 1100 °C at 10 °C/min is illustrated in (h).

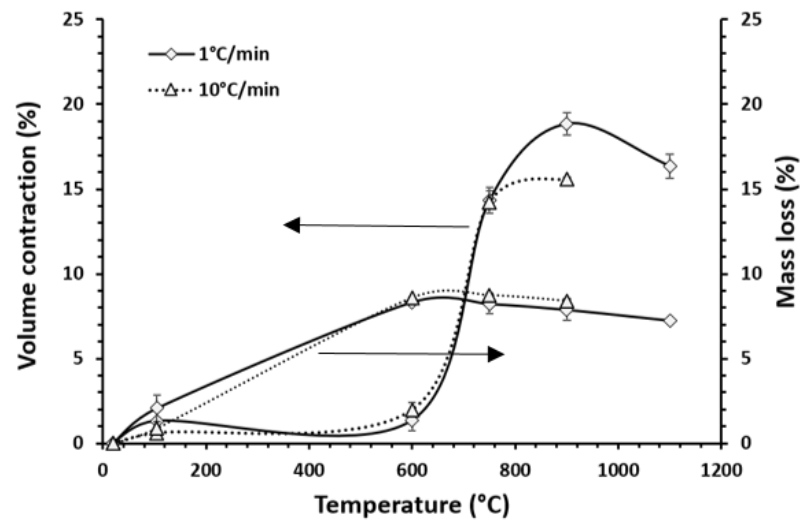


Figure 3. Mortars' volume contraction and mass loss as a function of temperature and heating rate. The curves are drawn as a guide to the eye. Due to deformation of the samples fired at 1100 °C with a heating rate of 10 °C/min data could not be collected.

When a higher heating rate was employed (10 °C/min), less distinguishable color changes were observed. The specimens heated up to 750 and 900 °C presented a less vivid brownish color relative to the ones heated at lower heating rates. Some color gradients were observed across the specimens' surfaces, especially when heated to 900 °C. The differences in color indicate that temperature gradients may have led to uneven transformations as suggested elsewhere [24]. In addition, some cracks and superficial degradation were visible on the surface of samples. The rapid increase of temperature accelerates dehydration processes, but water release occurs at higher temperatures due to lower heat and mass transfer rates (Figure 3), giving less time for steam to escape, which in turn results in excessive vapor pressure and leads to crack propagation [15]. Khan et al. [23] also reported severe cracks on Ca-rich fly ash/GGBFS mortars fired at 5 °C/min, suggesting some similarities in the effects of increased heating rates. However, all samples heated up to 900 °C maintained their structural integrity, regardless of the heating rate used. The samples heated to up 1100 °C with a heating rate of 10 °C/min present considerable molten material on their bottom surfaces (rotated in Figure 2h). Apart from the excessive vapor pressure generated, the large temperature gradients across the samples' cross-sections resulted in differential shrinkage, which increased the stresses formed and crack propagation (Figure 4), allowing for the runoff of molten material. Similar findings were reported by Fernández-Jiménez et al. [26], who observed that high heating and cooling rates form new or intensified pre-existing cracks due to the high thermal strain generated, ultimately leading to local failure. The viscosity of the melts also decreases as the temperature rises, which further facilitates their flow. Hence, the amount of molten material is expected to be significant at temperatures higher than 900 °C, as the increased flowability of the melts and the high number of voids and cracks in the mortar structures resulted in molten material coming out of the surfaces, as seen in Figures 2h and 4.



Figure 4. The surface of alkali activated mortar after thermal exposure to 1100 °C with heating rates of 10 °C/min. Molten material was removed from the sample surface for clarity.

In samples heated to 1100 °C with a lower heating rate, no molten material was visible after thermal exposure. The more gradual heating process diminished crack formation, which allowed the molten material to be retained inside the monolith, positively affecting the mortars' structural stability and high-temperature performance. Although mortars heated up to 1100 °C with heating rates of 10 °C/min retain their cubic shape and were tested for their compressive strength, they were excluded from further physical analysis (e.g., mass loss). The physical and mineralogical modifications that occurred upon heating had clear repercussions on AAMs' residual properties. From room temperature to 600 °C a slight increase of compressive strength after thermal exposure was observed, as shown by Figure 5.

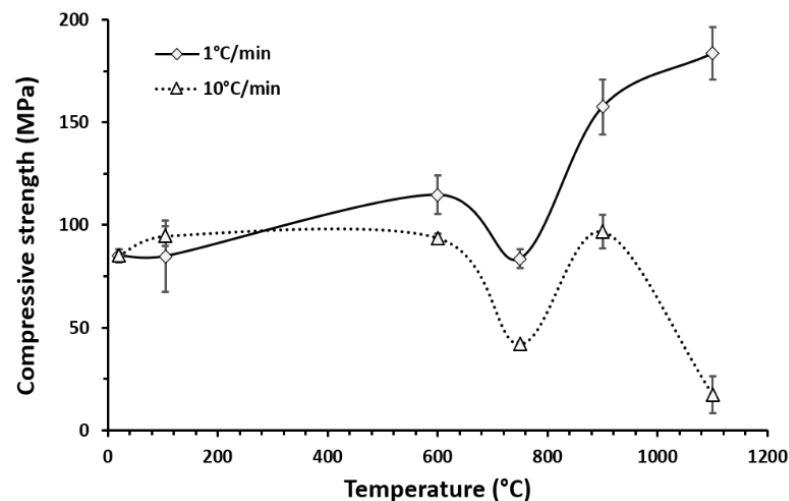


Figure 5. Mortars' compressive strength as a function of temperature and heating rate. The curves are drawn as a guide to the eye.

The improvement of compressive strength after thermal exposure to temperatures that do not exceed 600 °C is not related to melting and crystallization processes (see Section 3.3), but most likely to the increment of on-going polymerization reactions. In previous work [27,28], the authors have shown that in very similar alkali-activated systems, exothermic reactions have not completely ceased after more than 20 d of curing. Elevated temperatures stimulate these late-stage reactions and prompt the formation of more mechanically resistant binding phases. Along with the absence of significant crack formation, this beneficial effect overcomes the deleterious impact of dehydration and improves AAMs' mechanical features. The increase of compressive strength in this temperature range is often associated with densification [7,29]. However, it can be seen in Figure 6 that the

apparent density slightly decreases at 600 °C. Although more resistant and probably denser polymeric chains have been formed, this decrease is the combined effect of water loss and shrinkage. As mass loss (≈ 8.5 wt.%) was significantly higher than the volumetric contraction up to 600 °C (< 2 vol%), apparent densities decrease slightly. The increment of on-going reactions is further supported by comparing the mechanical strength of samples thermally treated up to 600 °C with different heating rates. As can be seen, lower heating rates—meaning more prolonged residence time at elevated temperatures—favor the formation of more resistant AAMs without significantly modifying the samples' mass and volume (Figure 3) or promoting the significant formation of new crystalline phases (Figure 7). At 750 °C, considerable deterioration of AAMs' mechanical properties occurred with both heating rates. This process may be related with modifications on the iron- and aluminosilicate networks occurring even before sintering [30]. The shrinkage of the aluminosilicate network induces internal cracks and increases the mean pore size, which leads to poorer mechanical performances [30]. Nonetheless, totally dehydrated charge balance cations (Na^+ or K^+) act as flux at high temperatures and reduce the temperature at which melting and crystallization start. This can imply the formation of partially sintered phases at around 750 °C [26]; however, these are not fully able to compensate for the decline in compressive strength caused by dehydration-related shrinkage.

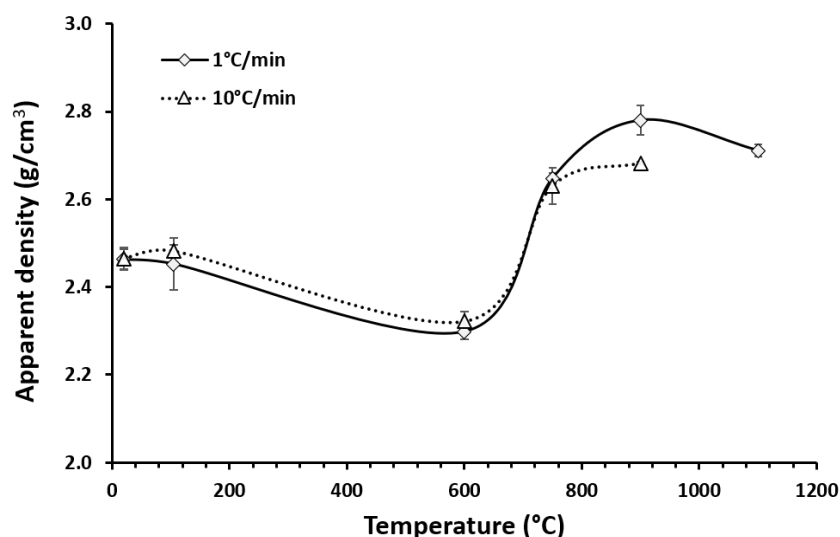


Figure 6. Mortars' apparent density as a function of temperature and heating rate. The curves are drawn as a guide to the eye. Due to deformation of the samples fired at 1100 °C with a heating rate of 10 °C/min data collection was not possible.

An additional factor that has been reported to contribute to the loss of strength at temperatures around 800 °C is the expansion of coarse aggregates [31]. Due to the type and granulometric distribution of the amorphous aggregates used in this work, however, a similar phenomenon seems unlikely to be significant. The effects of the network shrinkage could be seen at the macroscopic level by the steepest increase in volumetric contraction observed around 750 °C (Figure 3). At this temperature, increasing the heating rate was found to be detrimental to AAMs' residual strength. Along with higher crack formation due to the higher vapor pressure generated, the considerable difference in mechanical performance between mortars heated at different rates may indicate more deteriorated network structures. At 750 °C, AAMs start to lose their predominantly amorphous character, leading to the appearance of some broadened peaks of magnetite (Fe_3O_4) and esseneite (CaAlFeSiO_6) (Figure 7). These crystals could not be clearly identified in morphological analysis and does not seem able to compensate for the decrease of AAMs' mechanical strength; however, they may have contributed to some degree to the densification of the samples. As mass loss was mainly associated with dehydration processes occurring mostly

before 300 °C, the mass remained practically unchanged at temperatures higher than 600 °C. Therefore, the apparent density followed a similar trend to the volumetric contraction. A minor increase of mass was visible from 750 °C and above (Figure 3) that can be attributed to further oxidation and crystallization of iron species into magnetite and afterwards to hematite. The reference mortar presented a density of $2.46 \pm 0.02 \text{ kg/m}^3$ and a compressive strength of $85 \pm 3 \text{ MPa}$ after 28 d of curing. Using a heating rate of $1 \text{ }^\circ\text{C/min}$ the maximum apparent density was observed at 900 °C ($2.78 \pm 0.03 \text{ g/cm}^3$); however, the decrease of apparent density by 1100 °C was not detrimental to mechanical performance as the samples resulting from a heating rate of $1 \text{ }^\circ\text{C/min}$ presented the maximum compressive strength recorded, $184 \pm 13 \text{ MPa}$ (Figure 5).

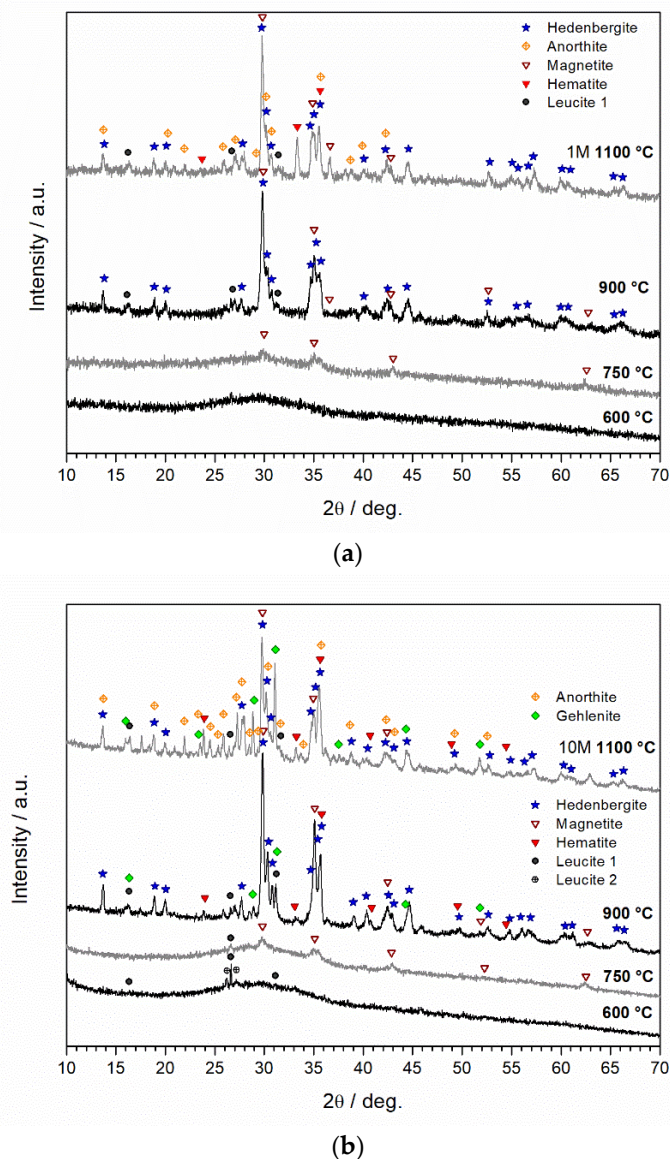


Figure 7. XRD patterns of alkali activated mortars after heating to different temperatures: (a) with a heating rate of $1 \text{ }^\circ\text{C/min}$; (b) with a heating rate of $10 \text{ }^\circ\text{C/min}$.

In those samples, when the temperature exceeded 750 °C and the crystallization of new phases became more intense, the compressive strength decrease was fully reversed. The compressive strength of sintered samples was progressively increased as the temperature rose, with an increase relative to the parent mortar of 85% and 115% at 900 and 1100 °C, respectively. Such strength gains contrast with the losses reported by several authors in low-iron systems, with proclivity towards lower mechanical performances as

the temperature rises [23,32]. Saxena et al. [32] investigated the influence of the Si/Al ratio in the thermal performance of fly ash geopolymer mortars and reported losses in compressive strength ranging from 54–77% when firing at 1000 °C. Conversely, Villaquirán-Caicedo and de Gutiérrez [33] reported significant increases in the mechanical strength of metakaolin geopolymers, but the maximum strength reported was approximately 160 MPa and required firing at 1200 °C for 2 h.

Increasing the heating rate to 10 °C/min not only provoked a higher decrease of compressive strength at 750 °C, but also significantly impaired the performance recovery at higher temperatures. On those samples, the maximum compressive strength was halved (97 ± 8 MPa) and attained at 900 °C. Despite the recovery from the decay observed at 750 °C and the 13% increase relative to the parent mortar, much higher compressive strengths were observed in samples heated up to 900 °C with the lower heating rate (158 ± 13 MPa). At 1100 °C, the mechanical strength of samples heated with different heating rates became even more divergent. Unlike samples heated at 1 °C/min that yielded the maximum strength at this temperature, when high heating rates were imposed, a considerable degradation of the AAMs' performance occurred. As shown in Figure 3, these samples were not dimensionally stable, with some molten material coming out of the samples' structure. This explains the much lower compressive strength. The reason for material run-off in some rapid heated samples might be that crystallization is not fast enough, while the viscosity decreases due to the increasing temperature. At the same time, capillary forces generated at the solid surface may further favor some material outflow from the molten core. At 1 °C/min, there seems to be a better match between the heating and crystallization rate, as the significant residence time and formation of more liquid phases does not promote such phenomena. With the exception of samples exposed to 1100 °C with a heating rate of 10 °C/min (17 ± 9 MPa), all sintered samples presented compressive strength values higher than 40 MPa.

3.2. Crystallinity

The mineralogical composition and the high-temperature mineralogical transitions are of utmost importance to fully describe the thermal behavior of AAMs and to safely classify them in terms of high-temperature resistance. At room temperature, AAMs are predominantly amorphous to semi-crystalline materials, and the amount and type of crystalline phases present are mainly dependent on the parent precursors. The powdered slag (PS) and silica fume (SF) used in this work as starting materials were almost completely XRD amorphous materials. Only one crystalline peak of small intensity was detected in the XRD patterns for SF, identified as moissanite (SiC) which was an impurity (SF and PS XRD patterns available in [27]).

Not surprisingly, the AAMs made thereof exhibited an entirely amorphous structure at room temperature, with a pronounced hump between 20–40° 2 θ in their XRD patterns. Heating the samples to 105 °C did not lead to any crystallization regardless of the heating rate used (not shown here for the sake of brevity). The first signs of the formation of crystalline phases were visible in the samples heated at 600 °C. Operating at the heating rate of 1 °C/min, no crystalline peak could be detected, as shown by Figure 7a; however, increasing the heating rate to 10 °C/min likely promoted the formation of some crystalline phases, visible from the peaks at 2 θ ~26–28° (Figure 7b). Given the weakness of the signals, a clear identification is impossible, but the positions are consistent with the main diffraction lines of leucite (KAlSi₂O₆) polymorphs (Leucite 1, PDF#76-2298, and Leucite 2, PDF#85-1626). Leucite is a well-known product of the thermal transformation of K-based AAMs [9].

The formation of crystalline phases was more pronounced as the temperature increased, stimulated by the separation of iron oxide phases. As with many waste-derived iron-rich glass-ceramic systems [34,35], a temperature increase to 750 °C involved the precipitation of magnetite (Fe₃O₄, PDF#89-0951), whereas a pyroxene phase (esseneite, PDF#78-1546), i.e., an Al-doped calcium-iron silicate, crystallized at 900 °C. Magnetite, embedding iron in both Fe²⁺ and Fe³⁺ forms (Fe₃O₄=FeO·Fe₂O₃), is a typical nucleating agent, separating at 650–800 °C from 'basaltic' glasses (glasses of the SiO₂-Al₂O₃-Fe₂O₃-

CaO system, including also alkali oxides), later transformed into pyroxene glass-ceramics. Magnetite may persist or be reabsorbed in the solid solution [34].

Heating to 900 °C and above promoted some oxidation, shown by the fact that both additional phases detected, i.e., CaAlFeSiO_6 (PDF#78-1546) and hematite (Fe_2O_3 , PDF#89-0599) host only Fe^{3+} ions [34]. Finally, it can be noted that the different heating rates determined a different evolution at the maximum temperature (1100 °C), with the appearance of calcium aluminosilicate phases: while the sample heated at 1 °C/min exhibited a limited precipitation of anorthite ($\text{CaAl}_2\text{Si}_2\text{O}_8$, PDF#73-0264), the sample heated at 10 °C/min featured both anorthite and gehlenite ($\text{Ca}_2\text{Al}_2\text{SiO}_7$, PDF#72-2128). Differences in the phase assemblage, with consequences for the thermo-elastic stresses developed upon cooling, could be a further explanation for the lower strength of samples heated at 10 °C/min: in particular, gehlenite is recognized for its high coefficient of thermal expansion [36].

The formation of eseneite and magnetite as the predominant phases in all samples can be seen as a natural consequence of the abundant availability of Si, Ca, and Fe species provided by the mix design. The addition of silica fume and potassium silicate solution could promote the formation of these thermally stable and refractory phases, which favor the formation of AAMs with high thermal performance [6,7,9,10,14]. The residual properties of the developed materials were enhanced with the adoption of slower heating rates. The physico-mechanical phenomena that occurred during faster heating processes, such as the higher vapor pressure and increased shrinkage and degradation of binding phases, seem to overwhelm possible positive effects from crystal formation. To further investigate such phenomena, morphological analyses were performed in samples heated up to 1100 °C, where the most significant crystallographic differences were observed.

3.3. Morphological Analysis

Figure 8 shows representative backscattered electron imaging micrographs of the reference mortar before being exposed to thermal treatment. A binder phase was formed (Figure 8a), but the existence of embedded unreacted particles confirms that complete dissolution was not achieved. The high solid-to-liquid ratio used (2.85) limited the precursors' dissolution, but the samples show a homogeneous matrix in which undissolved particles acted as small-sized aggregates, (Figure 8b). Extensive microcracks have been observed with undissolved particles acting as physical barriers that limited crack development and propagation. Similar microcracks have been reported in the literature, and their origin associated with drying shrinkage processes [28]. EDS analyses revealed a binder phase predominantly composed of Si, Al, Fe, Ca, and K, while the spectrum of undissolved particles was in line with the chemical composition of the slag used as the main precursor and as aggregates (Table 3). Some spherical pores were also observed that can be attributed to entrapped air during mixing.

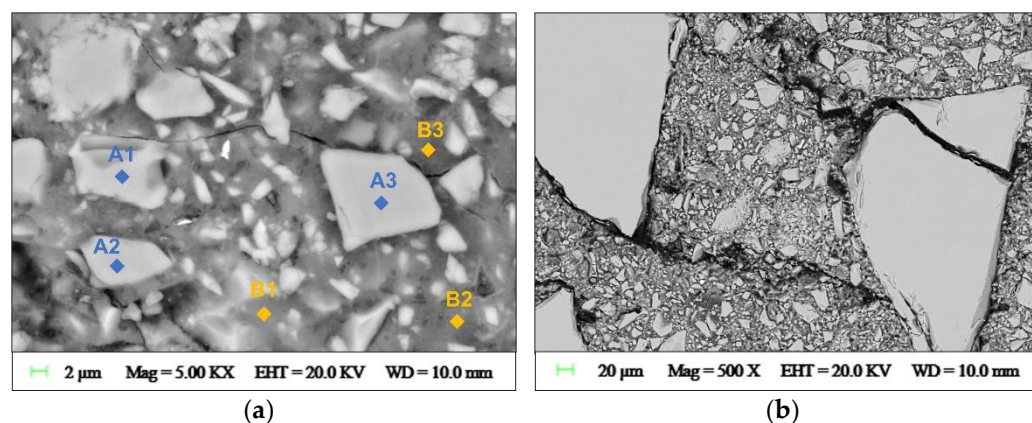


Figure 8. Backscattered electron imaging micrographs of alkali activated mortar before being exposed to elevated temperatures showing: (a) binder phase; (b) microcracks.

Table 3. Representative SEM-EDS results describing the chemical composition of binder and aggregates at room temperature (B1–B3, and A1–A3, respectively) and white areas outlining the aggregates’ contours after thermal exposure to 1100 °C (F1–F3). Data collection location as indicated in Figures 8a and 9b.

	SiO ₂	CaO	FeO _x	Al ₂ O ₃	MgO	TiO ₂	K ₂ O	Na ₂ O	Others
B1	44.6	13.8	18.8	14.4	1.0	0.7	6.2	0.5	0.0
B2	44.9	13.7	18.4	12.7	1.0	0.5	8.8	-	0.0
B3	46.3	10.5	20.2	13.0	1.0	-	8.4	0.6	0.0
A1	34.7	22.9	23.0	16.8	1.4	0.5	0.6	-	0.1
A2	34.2	23.6	23.1	16.4	1.3	0.6	0.6	-	0.2
A3	34.2	23.5	23.2	16.4	1.4	0.7	0.6	-	0.0
F1	11.5	7.8	73.2	5.8	Nd	0.7	-	-	1.0
F2	9.2	6.2	77.6	4.8	0.7	1.4	-	-	0.1
F3	11.8	9.6	72.4	4.5	0.7	0.7	-	-	0.3

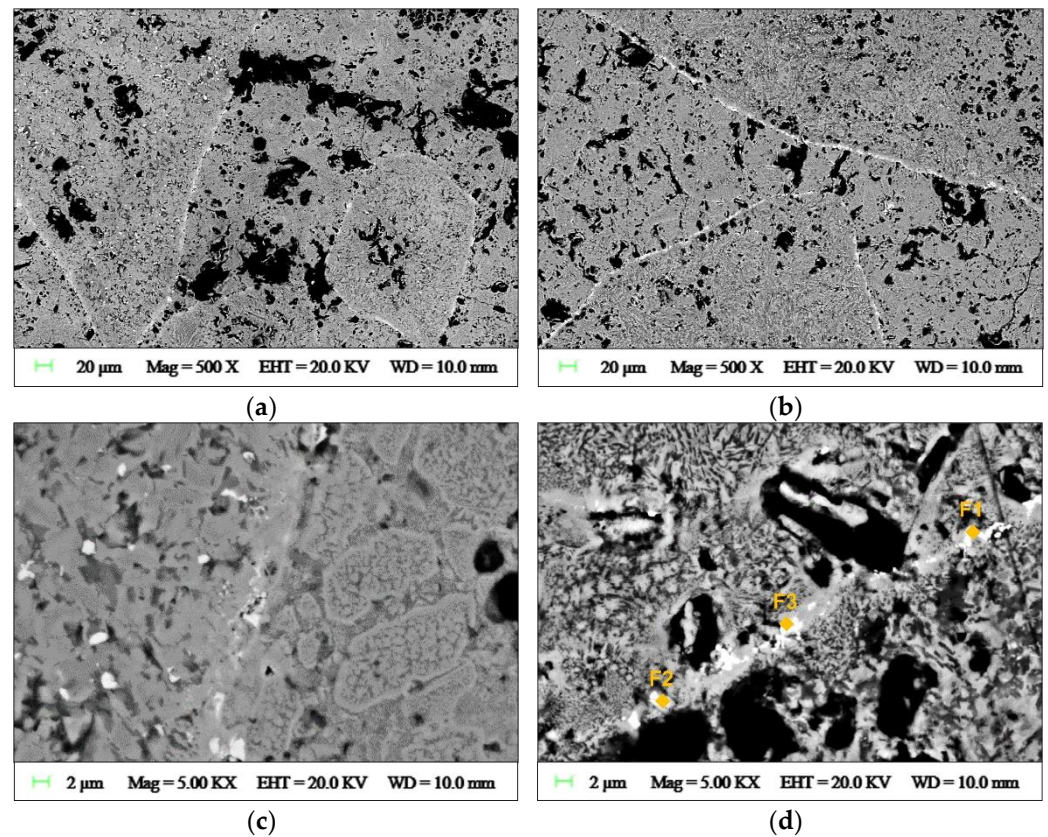


Figure 9. Backscattered electron imaging micrographs of mortars exposed to 1100 °C: (a,c) with a heating rate of 1 °C/min; (b,d) with a heating rate of 10 °C/min.

The effects of high-temperature exposure and heating rate on mortar morphology are illustrated in Figure 9. Independently of the heating rate used, a more compact microstructure with few large cracks was formed relative to the parent mortar. Partial softened aggregates have been reported to contribute to form homogenous mortars [23] and morphological analysis indicates that undissolved particles previously visible in green samples were almost completely molten (Figure 9a,b). Their previous homogeneous structure was transformed into a texture of finely exsolved phases. However, the contours of undissolved particles remain identifiable as white lines. A clearer picture of interfacial transition zones between molten aggregates and previous existing binders is better seen at higher magnification (Figure 9c,d). EDS analyses revealed the predominance of iron elements in

the white areas outlining the aggregates' contours, which suggests the concentration of oxidized iron phases at these locations (Table 3 and Figure 9d). At higher magnifications, the morphological differences between samples heated with distinct heating rates become more evident.

Mortars heated at 1 °C/min exhibit a continuous interfacial transition zone with no visible cracks or microscopic pores. The progressive increase in temperature that reduces vapor pressure and cracks formed upon heating, the prolonged residence time at high temperatures that may have increased the amount of molten material, and the use of potassium-based activating solutions that assist the formation of very viscous vitreous phases [26] may have all contributed to sealing pre-existing pores and cracks. More homogeneous microstructures were formed, in agreement with the enhanced compressive strength of these mortars after being exposed to high temperatures (Figure 3).

At the highest heating rate (Figure 9d), the thermal strains generated upon heating were more difficult to absorb by the existing microstructure at room temperature. Apart from the already mentioned local failure and runoff of molten material, the formation of micropores along interfacial transition zones was also visible. A less compact and more heterogeneous structure was formed at the microscopic level, and the less effective bonding between the newly crystallized phases can explain the lower mechanical strength of mortars heated at 10 °C/min at all temperatures above 600 °C.

These differences in the mortars' morphology show that heating rate plays a vital role in the sintering process. Increasing the heating rate affects not only the phases crystallized but also their morphology and distribution, which in turn affects the dimensional stability of the mortars at high temperatures and their properties after cooling. The crystallization of new phases was particularly relevant at temperatures over 900 °C, but strength only increased if a low heating rate was employed. Nevertheless, all mortars were able to largely surpass the threshold temperature of 400 °C without any visible signs of degradation or spalling. This behavior clearly shows the superior thermal performance of the developed products relative to mainstream construction materials.

4. Conclusions

In this work, the effect of temperature and heating rate on the post-heated properties of CaO-FeO_x-Al₂O₃-SiO₂-rich AAMs was investigated. The mix design of the AAMs employed a high content of a low-value residue (85.9 wt.%). This was driven by the aim to reduce the production cost and environmental impact of the produced materials, thus providing an up-cycling solution for the large volumes of CaO-FeO_x-Al₂O₃-SiO₂-rich slags generated in thermochemical conversion processes.

The results demonstrated the superior thermal performance of AAMs produced from these residues relative to mainstream construction materials and acknowledged the vital role of both of temperature and heating rate. Lower heating rates had a beneficial effect on AAMs' mechanical performance. The maximum strength was observed when specimens were exposed to 1100 °C at 1 °C/min (184 ± 13 MPa), more than doubling the compressive strength of green mortars (85 ± 3 MPa). Increasing the heating rate from 1 to 10 °C/min was found to promote deterioration processes that resulted in extensive crack development and even the deformation of samples at 1100 °C. Along with the formation of less homogeneous microstructures, these deleterious effects were found to result in more fragile structures after thermal exposure, which limits sintering to 900 °C if high heating rates are involved.

Crystallographic analyses revealed the crystallization of thermally stable phases, indicating that the refractory and high-temperature resistant features of the developed CaO-FeO_x-Al₂O₃-SiO₂-rich AAMs could be potentially further enhanced by fine-tuning the mix design.

Comparing to benchmark materials based on OPC, no signs of spalling were visible, and the developed materials could withstand temperatures up to 900 °C with heating rates up to 10 °C/min while maintaining their structural integrity and considerable mechanical strength (>40 MPa).

Author Contributions: Conceptualization, G.A.; methodology, G.A.; validation, G.A.; formal analysis, G.A., M.S., J.V.D.S., H.R., E.B. and Y.P.; investigation, G.A.; resources, F.F., M.M., E.B. and Y.P.; data curation, G.A.; writing—original draft preparation, G.A.; writing—review and editing, F.F., M.M., M.S., J.V.D.S., H.R., E.B. and Y.P.; visualization, G.A.; supervision, F.F., M.M. and Y.P.; project administration, F.F., M.M. and Y.P.; funding acquisition, F.F., M.M., E.B. and Y.P. All authors have read and agreed to the published version of the manuscript.

Funding: This research was funded by the European Union’s EU Framework Programme for Research and Innovation Horizon 2020 [Grant Agreement No 721185]. G.A.’s work was also supported by the Foundation for Science and Technology (FCT)—Aveiro Research Centre for Risks and Sustainability in Construction (RISCO), Universidade de Aveiro, Portugal [FCT/UIDB/ECI/04450/2020]. This publication reflects only the author’s view, exempting the Community from any liability. Project website: <https://new-mine.eu/> (accessed on 6 January 2022).

Institutional Review Board Statement: Not applicable.

Informed Consent Statement: Not applicable.

Data Availability Statement: Not applicable.

Acknowledgments: The authors wish to thanks to P. Rabelo Monich for her assistance in performing the high temperature tests.

Conflicts of Interest: The authors declare no conflict of interest. The funders had no role in the design of the study; in the collection, analyses, or interpretation of data; in the writing of the manuscript, or in the decision to publish the results.

References

- Machiels, L.; Arnout, L.; Yan, P.; Jones, P.T.; Blanpain, B.; Pontikes, Y. Transforming Enhanced Landfill Mining Derived Gasification/Vitrification Glass into Low-Carbon Inorganic Polymer Binders and Building Products. *J. Sustain. Met.* **2017**, *3*, 405–415. [CrossRef]
- Machiels, L.; Arnout, L.; Jones, P.T.; Blanpain, B.; Pontikes, Y. Inorganic Polymer Cement from Fe-Silicate Glasses: Varying the Activating Solution to Glass Ratio. *Waste Biomass Valorization* **2014**, *5*, 411–428. [CrossRef]
- Kriskova, L.; Pontikes, Y. Effect of activating solution on the synthesis and properties of porous Fe-Si-Ca-Rich inorganic polymers. In Proceedings of the 5th International Slag Valorisation Symposium, Leuven, Belgium, 3–5 April 2017; pp. 449–452. Available online: <http://slag-valorisation-symposium.eu/2017/wp-content/uploads/downloads/Session%206/Lubica%20Kriskova%20-%20Paper%20%20Effect%20of%20activating%20solution%20on%20the%20synthesis%20and%20properties%20of%20porous%20Fe-Si-Ca-rich%20inorganic%20polymers%20%20SVS2017.pdf> (accessed on 6 January 2022).
- Hertz, K. Limits of spalling of fire-exposed concrete. *Fire Saf. J.* **2003**, *38*, 103–116. [CrossRef]
- Rossino, C. Intrinsic Damage and Spalling Sensitivity of Concrete Subjected to High Temperature. Ph.D. Thesis, Politecnico di Milano, Milan, Italy, 2014.
- Kong, D.; Sanjayan, J.; Sagoe-Crentsil, K. Factors affecting the performance of metakaolin geopolymers exposed to elevated temperatures. *J. Mater. Sci.* **2008**, *43*, 824–831. [CrossRef]
- Van De Sande, J.; Pontikes, Y.; Rahier, H. Thermal Behaviour of Inorganic Polymers Synthesised from Fe-Rich Slags. In Proceedings of the Euroslag 2019 10th European Slag Conference, Thessaloniki, Greece, 8–11 October 2019; pp. 260–269.
- Flesoura, G.; Peys, A.; Vleugels, J.; Pontikes, Y. Alkali Activation of Synthetic SiO₂-CaO-FeOx-Al₂O₃-MgO Glass. In Proceedings of the 6th International Slag Symposium, Leuven, Belgium, 2–4 April 2019; pp. 411–414.
- Sakkas, K.; Pnias, D.; Nomikos, P.; Sofianos, A. Potassium based geopolymer for passive fire protection of concrete tunnels linings. *Tunn. Undergr. Space Technol.* **2014**, *43*, 148–156. [CrossRef]
- Pnias, D.; Balomenos, E.; Sakkas, K. The fire resistance of alkali-activated cement-based concrete binders. In *Handbook of Alkali-Activated Cements, Mortars and Concretes*; Elsevier: Amsterdam, The Netherlands, 2015; pp. 423–461.
- White, C.; Provis, J.L.; Proffen, T.; Van Deventer, J.S.J. The Effects of Temperature on the Local Structure of Metakaolin-Based Geopolymer Binder: A Neutron Pair Distribution Function Investigation. *J. Am. Ceram. Soc.* **2010**, *93*, 3486–3492. [CrossRef]
- Park, S.; Pour-Ghaz, M. What is the role of water in the geopolymerization of metakaolin? *Constr. Build. Mater.* **2018**, *182*, 360–370. [CrossRef]
- Sakkas, K.; Nomikos, P.; Sofianos, A.; Pnias, D. Utilisation of FeNi-Slag for the Production of Inorganic Polymeric Materials for Construction or for Passive Fire Protection. *Waste Biomass Valorization* **2014**, *5*, 403–410. [CrossRef]
- Bell, J.L.; Driemeyer, P.E.; Kriven, W.M. Formation of Ceramics from Metakaolin-Based Geopolymers. Part II: K-Based Geopolymer. *J. Am. Ceram. Soc.* **2009**, *92*, 607–615. [CrossRef]
- Degirmenci, F.N. Freeze-Thaw and fire resistance of geopolymer mortar based on natural and waste pozzolans. *Ceram. Silik.* **2017**, *62*, 41–49. [CrossRef]

16. Pnias, D.; Giannopoulou, I.; Sakkas, K. Utilisation of slag for the development of fire resistant geopolymers. In Proceedings of the 6th International Slag Valorisation Symposium, Leuven, Belgium, 2–4 April 2019; pp. 387–390.
17. Close, P.; Shepherd, H.M.; Drummond, C.H. Determination of Several Valences of Iron, Arsenic and Antimony, and Selenium in Glass. *J. Am. Ceram. Soc.* **1958**, *41*, 455–460. [[CrossRef](#)]
18. Morsy, M.S.; Shebl, S.S.; Rashad, A.M. Effect of fire on microstructure and mechanical properties of blended cement pastes containing metakaolin and silica fume. *Silic. Ind.* **2009**, *74*, 59.
19. Ascensão, G.; Seabra, M.P.; Aguiar, J.B.; Labrincha, J.A. Red mud-based geopolymers with tailored alkali diffusion properties and pH buffering ability. *J. Clean. Prod.* **2017**, *148*, 23–30. [[CrossRef](#)]
20. Hager, I.; Sitarz, M.; Mróz, K. Fly-ash based geopolymer mortar for high-temperature application—Effect of slag addition. *J. Clean. Prod.* **2021**, *316*, 128168. [[CrossRef](#)]
21. Zawrah, M.; Sadek, H.; Ngida, R.E.; Sawan, S.; El-Kheshen, A. Effect of low-rate firing on physico-mechanical properties of unfoamed and foamed geopolymers prepared from waste clays. *Ceram. Int.* **2022**, *in press*. [[CrossRef](#)]
22. EN 196-1:2016; Methods of Testing Cement. Part 1: Determination of Strength. BSI Standards Limited: London, UK, 2016; ISBN 978-0-58084-580-2.
23. Khan, N.N.; Sarker, P.K. Effect of waste glass fine aggregate on the strength, durability and high temperature resistance of alkali-activated fly ash and GGBFS blended mortar. *Constr. Build. Mater.* **2020**, *263*, 120177. [[CrossRef](#)]
24. Rickard, W.D.A.; van Riessen, A.; Walls, P. Thermal Character of Geopolymers Synthesized from Class F Fly Ash Containing High Concentrations of Iron and α -Quartz. *Int. J. Appl. Ceram. Technol.* **2010**, *7*, 81–88. [[CrossRef](#)]
25. He, R.; Dai, N.; Wang, Z. Thermal and Mechanical Properties of Geopolymers Exposed to High Temperature: A Literature Review. *Adv. Civ. Eng.* **2020**, *2020*, 7532703. [[CrossRef](#)]
26. Fernández-Jiménez, A.; Pastor, J.Y.; Martín, A.; Palomo, A. High-Temperature Resistance in Alkali-Activated Cement. *J. Am. Ceram. Soc.* **2010**, *93*, 3411–3417. [[CrossRef](#)]
27. Ascensão, G.; Marchi, M.; Segata, M.; Faleschini, F.; Pontikes, Y. Reaction kinetics and structural analysis of alkali activated Fe-Si-Ca rich materials. *J. Clean. Prod.* **2020**, *246*, 119065. [[CrossRef](#)]
28. Ascensão, G.; Beersaerts, G.; Marchi, M.; Segata, M.; Faleschini, F.; Pontikes, Y. Shrinkage and Mitigation Strategies to Improve the Dimensional Stability of CaO-FeOx-Al₂O₃-SiO₂ Inorganic Polymers. *Materials* **2019**, *12*, 3679. [[CrossRef](#)] [[PubMed](#)]
29. Duxson, P.; Lukey, G.C.; Van Deventer, J.S.J. Physical evolution of Na-geopolymer derived from metakaolin up to 1000 °C. *J. Mater. Sci.* **2007**, *42*, 3044–3054. [[CrossRef](#)]
30. Bakharev, T. Thermal behaviour of geopolymers prepared using class F fly ash and elevated temperature curing. *Cem. Concr. Res.* **2006**, *36*, 1134–1147. [[CrossRef](#)]
31. Kong, D.L.; Sanjayan, J.G. Effect of elevated temperatures on geopolymer paste, mortar and concrete. *Cem. Concr. Res.* **2010**, *40*, 334–339. [[CrossRef](#)]
32. Saxena, S.; Kumar, M.; Singh, N. Fire Resistant Properties of Alumino Silicate Geopolymer cement Mortars. *Mater. Today Proc.* **2017**, *4*, 5605–5612. [[CrossRef](#)]
33. Villaquirán-Cacedo, M.; de Gutiérrez, R.M. Synthesis of ceramic materials from ecofriendly geopolymer precursors. *Mater. Lett.* **2018**, *230*, 300–304. [[CrossRef](#)]
34. Höland, W.; Beall, G. *Glass-Ceramic Technology*; The American Ceramic Society: Westerville, OH, USA, 2002; p. 372.
35. Bernardo, E.; Esposito, L.; Rambaldi, E.; Tucci, A.; Pontikes, Y.; Angelopoulos, G. Sintered esseneite-wollastonite-plagioclase glass-ceramics from vitrified waste. *J. Eur. Ceram. Soc.* **2009**, *29*, 2921–2927. [[CrossRef](#)]
36. Bernardo, E.; Bonomo, E.; Dattoli, A. Optimisation of sintered glass-ceramics from an industrial waste glass. *Ceram. Int.* **2010**, *36*, 1675–1680. [[CrossRef](#)]